





**Bi<sub>2</sub>YbO<sub>4</sub>Cl: A two-dimensional square-lattice compound with  $J_{\text{eff}} = \frac{1}{2}$  magnetic moments**V. K. Singh <sup>1</sup>, K. Nam,<sup>2</sup> M. Barik,<sup>3</sup> K. Boya,<sup>1</sup> E. Kermarrec <sup>4</sup>, P. Khuntia,<sup>3,5</sup> Kee Hoon Kim,<sup>2</sup>  
S. Bhowal <sup>6,7,\*</sup> and B. Koteswararao <sup>1,†</sup><sup>1</sup>*Department of Physics, Indian Institute of Technology Tirupati, Tirupati 517506, India*<sup>2</sup>*Department of Physics and Astronomy and Institute of Applied Physics, Seoul National University, Seoul 151-747, Republic of Korea*<sup>3</sup>*Department of Physics, Indian Institute of Technology Madras, Chennai 600036, India*<sup>4</sup>*Université Paris-Saclay, CNRS, Laboratoire de Physique des Solides, 91405 Orsay, France*<sup>5</sup>*Quantum Centre of Excellence for Diamond and Emergent Materials, Indian Institute of Technology Madras, Chennai 600036, India*<sup>6</sup>*Materials Theory, ETH Zurich, Wolfgang-Pauli-Strasse 27, 8093 Zurich, Switzerland*<sup>7</sup>*Department of Physics, Indian Institute of Technology Bombay, Mumbai 400076, India*

(Received 29 October 2023; revised 12 January 2024; accepted 23 January 2024; published 13 February 2024)

The interplay between the quantum effects from low-dimensionality and the spin-orbit coupling leads to exotic ground states with unusual excitations. We report the structural, magnetic, heat capacity, and electronic structure studies of Bi<sub>2</sub>YbO<sub>4</sub>Cl, which constitutes a structurally perfect 2D square lattice with rare-earth magnetic Yb<sup>3+</sup> ions. The magnetization and heat capacity data analysis confirms that the Yb<sup>3+</sup> ion hosts the spin-orbit driven  $J_{\text{eff}} = \frac{1}{2}$  state at low temperatures. From the fit to the Curie-Weiss law on the magnetic susceptibility data in the low-temperature region, the observed Curie-Weiss temperature is about  $-1$  K, implying an antiferromagnetic (AFM) coupling between the Yb<sup>3+</sup> moments. The heat capacity data show the presence of a broad maximum at 0.3 K and the absence of any sharp magnetic anomaly down to 0.09 K, indicating the onset of short-range correlations. Our first-principles calculations based on density functional theory provide further insight into the role of the microscopic parameters. In particular, it points out the crucial role of spin-orbit coupling in driving both the  $J_{\text{eff}} = \frac{1}{2}$  state as well as the antiferromagnetic interaction between the nearest-neighbor Yb<sup>3+</sup> moments that is consistent with experimental results. The total energy calculations suggest an easy-axis (out-of-plane) anisotropy of the spins.

DOI: [10.1103/PhysRevB.109.075128](https://doi.org/10.1103/PhysRevB.109.075128)**I. INTRODUCTION**

Low-dimensional quantum magnetism has been an exciting research area since the discovery of high-temperature superconductivity (HTSC) in a hole or electron-doped two-dimensional (2D) copper-based Heisenberg antiferromagnetic (HAFM) square-lattice oxide ceramics [1]. The fundamental aspects of low-dimensional quantum magnetism are quite interesting due to the presence of substantial quantum fluctuations, which lead to novel quantum ground states and unusual excitations [2]. The Mermin-Wagner theorem states that no magnetic long-range order (LRO) can be stabilized at finite temperature in the isotropic low-dimensional Heisenberg model system [3]. The quantum fluctuations decay generally while increasing the dimensionality from one dimensional (1D) to three dimensional (3D). The 2D systems with moderate levels of quantum fluctuations show interesting quantum phase transitions [4]. Among the diverse 2D spin systems, the  $S = \frac{1}{2}$  2D square lattice has piqued the curiosity of researchers due to the possible connection with the HTSC. A few classes of 2D square-lattice materials, such as iron pnictides, tellurides, selenides, and nickelates, host the HTSC

under perturbations such as doping, pressure, etc. [5–8]. However, the cuprates still hold the highest  $T_c$  record at ambient pressure, which makes the research on  $S = \frac{1}{2}$  2D HAFM square lattice still an exciting prospect on both the theoretical and experimental fronts of condensed matter.

The  $S = \frac{1}{2}$  HAFM square lattice exhibits Néel LRO in the ground state at  $T = 0$  K with a reduction of about 40% of the staggered magnetic moment due to the influence of quantum effects [9]. The 2D square lattice exhibits resilience to the LRO at  $T > 0$  K due to the presence of substantial thermal and quantum fluctuations. A few famous experimental realizations for the 2D square-lattice materials that exhibit the magnetic LRO are La<sub>2</sub>CuO<sub>4</sub> [10,11], and Sr<sub>2</sub>CuO<sub>2</sub>Cl<sub>2</sub> [12,13], owing to the non-negligible interlayer interactions. Experimentally, the deconfined fractional quasiparticles were detected at high energies in other  $S = \frac{1}{2}$  2D square-lattice materials [14–17]. Subsequently, several theoretical models based on HAFM square-lattice systems were formulated to investigate numerous exotic states, such as resonant valence bond (RVB) or quantum spin liquid (QSL) [18–20]. Interestingly, the anisotropic nature of the spin changes the excitation spectrum with quantum entanglement features [21].

On the other hand, rare-earth magnets exhibit fascinating properties owing to their substantial spin-orbit coupling (SOC). Especially the Yb<sup>3+</sup> ion, which holds a  $J_{\text{eff}} = \frac{1}{2}$  state due to SOC and crystal electric field (CEF) effects [22]. The

\*sayantika.bhowal31j@gmail.com

†koteswararao@iittp.ac.in

anisotropic nature of magnetic exchange couplings between  $\text{Yb}^{3+}$  ions in the compounds often leads to many exotic ground state properties such as the realization of quantum spin ice in pyrochlore materials [23–26], and Tomonaga-Luttinger liquid behavior in spin-chain magnets with spinon confinement-deconfinement transitions [27]. The Yb-based honeycomb magnets are being explored as potential candidates to host Kitaev spin liquids [28–31]. Remarkably, the  $\text{Yb}^{3+}$ -based 2D triangular lattice materials with isotropic nearest-neighbor (NN) interaction have also received significant attention. While the 2D HAFM triangular lattice model predicts a  $120^\circ$  Néel LRO at  $T = 0$  K [32,33], the quantum spin-liquid (QSL) ground state has been identified experimentally in the compounds with 2D triangular networks  $\text{YbMgGaO}_4$ ,  $\text{NaYbO}_2$ ,  $\text{NaYbSe}_2$ , etc., possibly due to the presence of anisotropic interactions [34–37]. In the case of the HAFM  $S = \frac{1}{2}$  square-lattice model, the system exhibits Néel LRO in the ground state at  $T = 0$  K [15,38]. Compared to the 2D honeycomb and triangular magnets, the antiferromagnetism is expected to be robust in the case of square lattice due to the lack of Kitaev-type anisotropic and frustrated interactions, respectively. Studying the effect of SOC in a 2D square lattice with  $J_{\text{eff}} = \frac{1}{2}$  moments is thus an interesting fundamental problem in condensed matter physics. Recently, a 2D distorted square-lattice compound  $\text{NaYbGeO}_4$  has been investigated, showing a sharp magnetic transition at 0.21 K, and it is also noticed as the candidate material for the adiabatic demagnetization refrigeration at low temperatures [39]. Further, exploring the rare-earth magnetic material with a perfect 2D square-lattice magnetic system would be intriguing. For this purpose, the potential compound with a structurally perfect 2D lattice is identified for studying the SOC effects on the ground state.

In this paper, we report a detailed investigation of the  $J_{\text{eff}} = \frac{1}{2}$  magnetic lattice system  $\text{Bi}_2\text{YbO}_4\text{Cl}$ , where the spins  $\text{Yb}^{3+}$  are arranged on a 2D square lattice. The magnetic susceptibility data reveal the presence of strong SOC and CEF effects in  $\text{Bi}_2\text{YbO}_4\text{Cl}$  that result in a  $J_{\text{eff}} = \frac{1}{2}$  Kramer's doublet ground state at low temperatures. The heat capacity shows a broad maximum at  $T^{\text{max}} = 0.3$  K, which signifies the onset of short-range correlations. The absence of any sharp magnetic anomaly in the  $C_p$  data down to 0.09 K implies a quantum-disordered ground state. Our electronic structure calculations based on density functional theory (DFT) further show that the NN Yb- $f$  electrons interact within the plane, while the out-of-plane interaction is extremely weak, suggesting the presence of a 2D spin model in  $\text{Bi}_2\text{YbO}_4\text{Cl}$ . Additionally, our calculations underscore the significant role of spin-orbit interactions in driving the antiferromagnetic coupling between NN  $\text{Yb}^{3+}$  ions and also the formation of the  $J_{\text{eff}} = \frac{1}{2}$  state.

## II. METHODS

### A. Experimental techniques

The polycrystalline sample of  $\text{Bi}_2\text{YbO}_4\text{Cl}$  was synthesized using the hydrothermal synthesis technique. The high-purity chemicals of  $\text{BiOCl}$  (Aldrich, 99.99%) and  $\text{Yb}_2\text{O}_3$  (Aldrich, 99.99%) were used. We note that the  $\text{Yb}_2\text{O}_3$  chemical is pre-fired at  $1000^\circ$  to remove the moisture and absorbed  $\text{CO}_2$

before using it for the hydrothermal reaction. The starting materials of  $\text{BiOCl}$  (0.520 g) and  $\text{Yb}_2\text{O}_3$  (0.197 g) with the molar ratio Bi:Yb = 2:1 were dissolved in 100 ml of deionized water. The mixture obtained without any homogenization was then directly transferred into a 150-ml Teflon-lined stainless-steel autoclave and heated to and held at  $180^\circ\text{C}$  for three days. The autoclave was then cooled down to room temperature. In order to get better-quality samples, we performed the hydrothermal treatment on the obtained powder from the previous attempt for another 24 hours. The single-phase purity of the sample was confirmed from the powder x-ray diffraction (XRD) measurements performed at room temperature, which is consistent with the reported data [40]. A PANalytical powder diffractometer with Cu- $K\alpha$  radiation ( $\lambda_{\text{avg}} \approx 1.5406 \text{ \AA}$ ) was used for the powder XRD experiment. Rietveld refinement analysis is done using the FullProf Suite software package [41]. The magnetic field and temperature-dependent magnetization measurements were performed on the polycrystalline samples of  $\text{Bi}_2\text{YbO}_4\text{Cl}$  using a superconducting quantum interference device (SQUID) attached to the magnetic property measurement system (MPMS) until 7-T magnetic field and down to a low temperature of 0.64 K. We have also measured magnetization using vibrating sample magnetometer (VSM) attached to physical property measurement system (PPMS) until 9-T magnetic field and down to the low temperature of 1.8 K. The heat capacity data from 1.8 K to 300 K is measured in various magnetic fields using the heat capacity option of the Dynacool PPMS from Quantum Design. The low-temperature heat capacity data down to 0.09 K in zero magnetic field were obtained by using a CF-150 dilution fridge (Leiden cryogenics) on the powder samples.

### B. Theoretical methods

The electronic structure of  $\text{Bi}_2\text{YbO}_4\text{Cl}$  is investigated using the linearized augmented plane wave (LAPW) method as implemented in the all-electron, full potential code ELK [42]. We have carried out both nonspin and spin-polarized electronic-structure calculations and also incorporated the effect of SOC within the LDA + SOC +  $U$  formalism with  $U_{\text{eff}} = 6$  eV for the correlated Yb- $f$  electrons [43,44]. A basis set of  $l_{\text{max(apw)}} = 9$  and a  $5 \times 5 \times 2$   $k$ -point sampling of the Brillouin zone are used to achieve the self-consistency. The product of the muffin-tin radius (2.8, 2.8, 1.8, and 2.2 a.u. for Bi, Yb, O, and Cl, respectively) and the maximum reciprocal lattice vector is taken to be 8.

## III. EXPERIMENTAL RESULTS AND ANALYSIS

### A. Structural analysis

The single phase of the sample is confirmed via powder XRD. Rietveld refinement of XRD data confirms the purity and good quality of the sample (see Fig. 1). The values for refinement are as follows:  $\chi^2 \approx 2.72$ ,  $R_p \approx 8.38\%$ ,  $R_{\text{wp}} \approx 8.86\%$ ,  $R_{\text{exp}} \approx 5.29\%$ . The obtained lattice parameters from the refinement at room temperature  $a = b = 3.82 \pm 0.02 \text{ \AA}$ ,  $c = 8.85 \pm 0.04 \text{ \AA}$ , and  $\alpha = \beta = \gamma = 90^\circ$  are in close agreement with a previous report [40]. The compound  $\text{Bi}_2\text{YbO}_4\text{Cl}$  crystallizes in the tetragonal space group  $P4/mmm$ . The crystal structure of the compound  $\text{Bi}_2\text{YbO}_4\text{Cl}$  is depicted in Fig. 2(a),

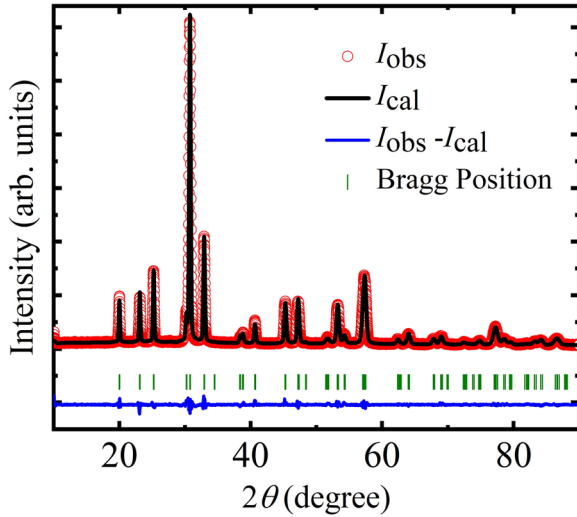


FIG. 1. Rietveld fit of the data at 300 K. The Bragg positions are shown with green vertical bars, and the solid blue line represents the difference between the experimental and calculated intensities.

where the edge-shared YbO<sub>8</sub> polyhedral units connect to form a well-separated 2D square-lattice network. The Yb<sup>3+</sup> resides in the slightly distorted environment of YbO<sub>8</sub>. The intra- and interplaner hopping integrals,  $t_{\alpha\beta}^{\text{intra}}$  and  $t_{\alpha\beta}^{\text{inter}}$ , between the Yb<sup>3+</sup> ions are indicated by curved lines. The NN intraplaner hopping  $t_{\alpha\beta}^{\text{intra}}$  along  $\hat{x}$  and  $\hat{y}$  are indicated in dashed and solid lines, respectively.

The NN Yb ions form a square lattice in the  $xy$  plane as represented in Fig. 2(c). The interlayer separation between two square layers ( $d_{\text{inter}}$ ) is about 8.85 Å [see Fig. 2(b)]. The intralayer Yb<sup>3+</sup>-Yb<sup>3+</sup> bond length ( $d_{\text{intra}}$ ) is 3.82 Å, as shown in Fig. 2(d). The 2D layers seem to be well separated, with a ratio  $d_{\text{inter}}/d_{\text{intra}}$  of 2.31. The intraplanar exchange interaction is mediated via the Yb-O-Yb path having an angle of 109.4°. The later sections will report the investigation of the exchange

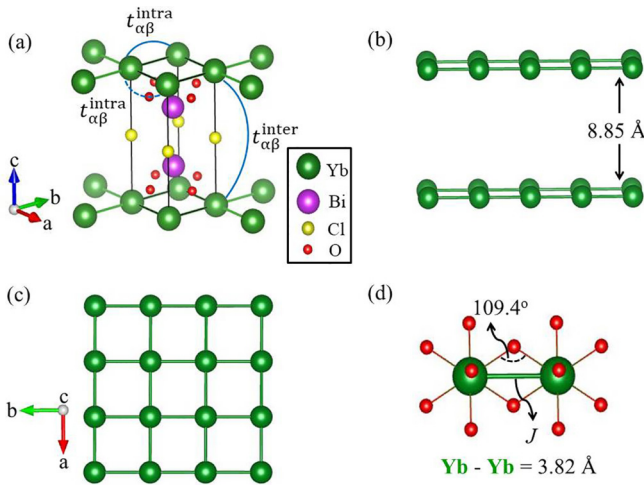


FIG. 2. (a) The crystal structure of Bi<sub>2</sub>YbO<sub>4</sub>Cl. (b) The interlayer separation is about 8.85 Å. (c) The depiction of a 2D square-lattice network. (d) The intrachain interaction path between first NN Yb atoms with bond angle and bond length.

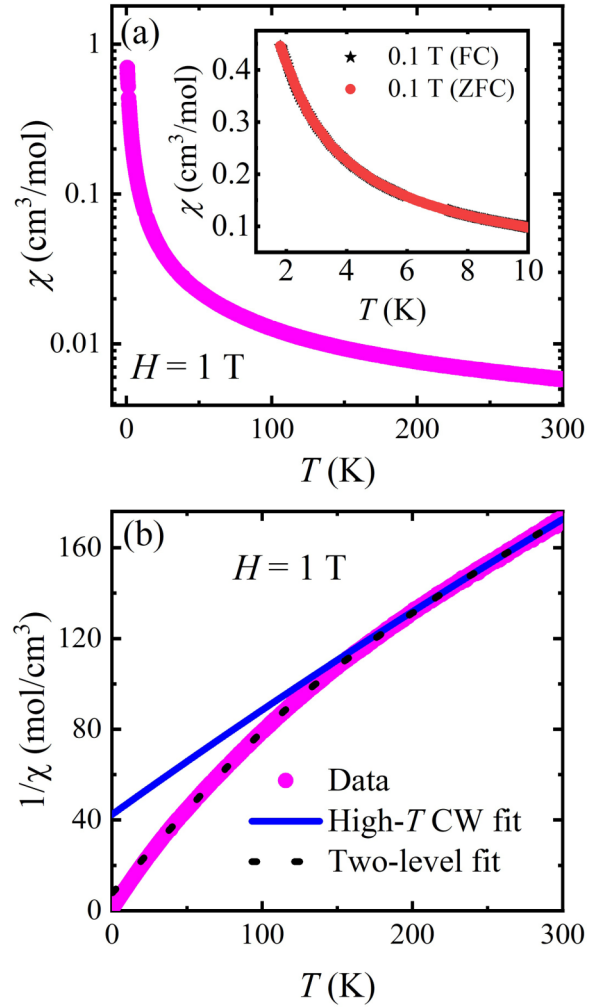


FIG. 3. (a) Temperature-dependent magnetic susceptibility  $\chi(T)$  measured in an applied field of 1 T. (Inset)  $\chi(T)$  measured at 0.1 T in ZFC and FC conditions. (b) Inverse susceptibility ( $1/\chi$ ) plot as a function of  $T$ . The solid (blue) line indicates the CW fit at the high- $T$  region, and the black dashed line denotes the two-level CW fit.

interactions and the role of SOC effects on the ground state. Overall, the compound Bi<sub>2</sub>YbO<sub>4</sub>Cl is a promising candidate for exploring 2D square-lattice physics.

## B. Magnetization measurements

Magnetization as a function of temperature and magnetic field measurements provide the ground-state nature of quantum magnets. The temperature-dependent magnetic susceptibility  $\chi(T)$  of the polycrystalline sample Bi<sub>2</sub>YbO<sub>4</sub>Cl at 1 T field is shown in Fig. 3(a). There is no signature of any anomaly or LRO down to 0.64 K in the  $\chi(T)$  data. The inset of Fig. 3(a) shows the zero-field cooled (ZFC) and field-cooled (FC) magnetic susceptibility data at 0.1 T. There is no bifurcation of ZFC and FC susceptibilities, which signifies the absence of spin freezing or spin glass transition at least down to 1.8 K. The inverse  $\chi(T)$  data above 180 K is fitted with the expression  $1/\chi = \frac{T - \theta_{CW}^{HT}}{C_{HT}}$  [see Fig. 3(b)]. Here, the  $\theta_{CW}^{HT}$  represents the Curie-Weiss (CW) temperature

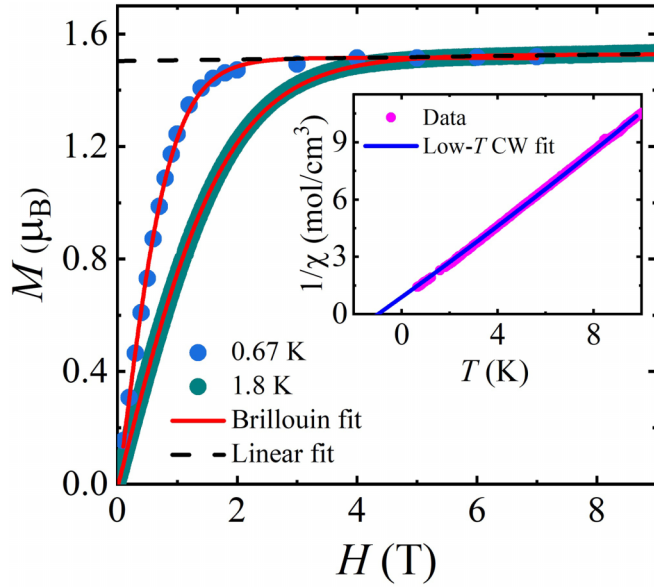


FIG. 4. Isothermal magnetization and Brillouin fit at different temperatures. The horizontal dashed line denotes the linear fit, which is extrapolated to a saturated magnetization. (Inset) The CW fit at low- $T$  region.

at the high-temperature region, and  $C_{HT}$  is the Curie constant. The extracted parameters from the high-temperature fit are  $\theta_{CW}^{HT} = -115 \pm 2$  K,  $C_{HT} = 2.45$  cm<sup>3</sup> K/mol. The effective moment is calculated from  $C_{HT}$  value using the formula  $\mu_{\text{eff}} = \sqrt{3k_B C / N_A} \approx \sqrt{8C} \mu_B$ , where  $N_A$  is Avogadro's number, and  $k_B$  is the Boltzmann constant. The obtained value of effective moment  $\mu_{\text{eff}} = 4.42 \mu_B$  is comparable to that anticipated for the Yb<sup>3+</sup> free ions ( $4f^{13}; L = 3, S = \frac{1}{2}, J = \frac{7}{2}$ ). We note that this large negative value of  $\theta_{CW}^{HT}$  does not represent the presence of antiferromagnetic interactions. The large negative value of  $\theta_{CW}^{HT}$  rather signifies the effect of the crystal electric field (CEF) excitations. In the case of Yb<sup>3+</sup> ions (with an odd number of electrons), the eightfold degenerate  $J = \frac{7}{2}$  multiplet split into four Kramers doublets due to the CEF effects. At the high  $T$ , the magnetic moment has significant contributions from thermally populated crystal field levels.

To obtain the information about the low-temperature state, the inverse  $\chi(T)$  data is fitted with the Curie-Weiss law,  $\chi(T) = \chi_o^{LT} + \frac{C_{LT}}{T - \theta_{CW}^{LT}}$ , in the temperature range 20–0.64 K [see inset of Fig. 4]. The temperature-independent  $\chi_o^{LT}$  term is the combination of core diamagnetic susceptibility and Van Vleck paramagnetic susceptibility. The  $C_{LT}$  and  $\theta_{CW}^{LT}$  denote the low-temperature values of the Curie constant and CW temperature, respectively. The fit gives  $\chi_o^{LT} \approx 2.24 \times 10^{-3}$  cm<sup>3</sup>/mol,  $\theta_{CW}^{LT} \approx -1 \pm 0.1$  K, and  $C_{LT} \approx 0.98$  cm<sup>3</sup> K/mol. The  $\chi_{\text{dia}}$  for the Bi<sub>2</sub>YbO<sub>4</sub>Cl sample is calculated by summing up the core diamagnetic susceptibilities of individual ions Bi<sup>3+</sup>, Yb<sup>3+</sup>, O<sup>2-</sup>, and Cl<sup>-1</sup> [45], which comes out to be  $-1.42 \times 10^{-4}$  cm<sup>3</sup>/mol. Deducting the calculated diamagnetic susceptibility from  $\chi_o^{LT}$  gives us the Van Vleck susceptibility of about  $2.63 \times 10^{-3}$  cm<sup>3</sup>/mol, which results from the second-order contribution to free energy in the presence of the magnetic field. The obtained value of Van Vleck susceptibility at low temperatures is consistent

with other Yb<sup>3+</sup> compounds [46–48]. The calculated value of effective magnetic moment comes out to be  $\mu_{\text{eff}} \approx 2.78 \mu_B$ . It is evident that the obtained value of an effective moment at low temperatures,  $\mu_{\text{eff}} \approx 2.78 \mu_B$  is significantly smaller than that of the high-temperature value  $\mu_{\text{eff}} \approx 4.54 \mu_B$ . As, we know the Yb<sup>3+</sup> ion, with  $J = 7/2$  comprises eight basis states, which upon exposure to a distorted CEF environment, Yb<sup>3+</sup> adheres to Kramer's theorem, causing the degenerate ground states to split. This splitting results in a maximum of four doublets with quantum numbers  $\pm 1/2, \pm 3/2, \pm 5/2$ , and  $\pm 7/2$ . The ground state of Yb<sup>3+</sup> at low temperatures adopts the  $J_{\text{eff}} = \pm 1/2$  doublet state. Further we extract the value of  $g$  from the magnetic moment formula  $\mu_{\text{eff}} = g\sqrt{J_{\text{eff}}(J_{\text{eff}} + 1)} \mu_B$  by fixing the value  $J_{\text{eff}} = \frac{1}{2}$ , which comes out to be 3.2.

To further understand the ground state of the titled material, the isothermal magnetization as a function of the magnetic field was carried out at low temperatures at 0.67 K and 1.8 K (see Fig. 4). The isothermal magnetization data is fitted with a linear equation above 5 T. The fit is extrapolated down to zero field to obtain the saturation magnetic moment value. The saturated magnetic moment comes out to be  $M_s = 1.45 \mu_B$ . After subtracting the diamagnetic contribution, the slope of the linear fit provides the value of Van Vleck's paramagnetic contribution  $2.8 \times 10^{-3}$  cm<sup>3</sup>/mol. In the paramagnetic state, we model the observed isothermal Magnetization with the following function,  $M(H) = \chi_o H + gJ_{\text{eff}} N_A \mu_B B_{J_{\text{eff}}}(H, T)$ , where  $B_{J_{\text{eff}}}(H, T)$  is the Brillouin function for  $J_{\text{eff}} = \frac{1}{2}$  [49]. The fit to the Brillouin function is shown at various temperatures in Fig. 4. The  $M(H)$  data very well matches with  $J_{\text{eff}} = \frac{1}{2}$  and  $g \approx 2.9$ . The result confirms the Yb<sup>3+</sup> ions possess spin-orbit entangled  $J_{\text{eff}} = \frac{1}{2}$  moment at low temperatures. In such cases, the low-temperature magnetic properties of Yb<sup>3+</sup> ions are primarily controlled by the exchange interactions between the  $J_{\text{eff}} = \frac{1}{2}$  moments, which are confined to the lowest Kramers doublet state. The influence of CEF on the Kramers doublet state can be approximated using the following two-level equation [50,51]:

$$\chi^{-1} = \chi_o^{-1} + 8(T - \theta_{CW}) \left( \frac{\mu_{\text{eff},1}^2 + \mu_{\text{eff},2}^2 \times e^{-\frac{\Delta_{CEF}}{T}}}{1 + e^{-\frac{\Delta_{CEF}}{T}}} \right)^{-1}. \quad (1)$$

Here,  $\Delta_{CEF}$  represents the energy splitting for the ground state and first excited state due to the influence of CEF. The effective magnetic moments associated with these CEF levels are  $\mu_{\text{eff},1}$ , and  $\mu_{\text{eff},2}$ , respectively. As shown in Fig. 3(b), the inverse magnetic susceptibility data is fitted to the two-level model, which provides the parameters as  $\chi_o = 1.13 \times 10^{-3}$  cm<sup>3</sup>/mol,  $\Delta_{CEF} = 360$  K,  $\theta_{CW} = -5$  K,  $\mu_{\text{eff},1} = 3.1 \mu_B$ , and  $\mu_{\text{eff},2} = 4.3 \mu_B$ . The large value of  $\Delta_{CEF}$  again suggests that the ground state is very well separated from its first excited state, as noticed in other Yb-based magnets [36,37,51]. It is to be noted that this two-level fit is a simplified model and qualitative method to estimate the value of the energy splitting between the ground state and the first excited crystal field level. To estimate the value of the CEF energy gaps precisely, inelastic neutron scattering (INS) or Raman spectroscopy would be required.

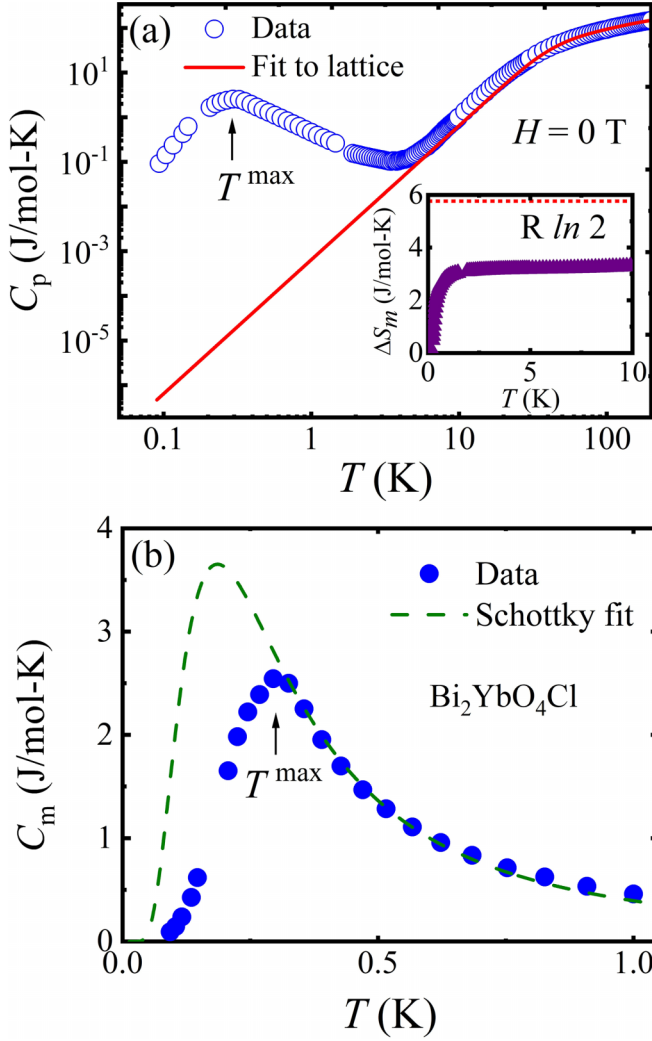


FIG. 5. (a).  $C_p$  vs  $T$  plot at 0 T, where the solid red line is fit to the lattice. (Inset) The value of entropy change  $\Delta S_m$  vs  $T$  at 0 T. The horizontal dotted red line indicates the expected  $\Delta S_m$  value for the spin  $\frac{1}{2}$  systems. (b) The extracted  $C_m$  vs  $T$  at 0 T with the two-level Schottky fit.

### C. Heat capacity

We measured the temperature dependence of heat capacity  $C_p(T)$  of the compound Bi<sub>2</sub>YbO<sub>4</sub>Cl down to 0.09 K in zero magnetic field to obtain more insight into the ground-state properties. Figure 5(a) shows the  $C_p(T)$  data in zero field, where no LRO is noticed down to 0.09 K, despite the antiferromagnetic interactions of about  $\theta_{CW} \approx -1$  K. Below 3 K, the magnetic contribution to heat capacity is prominent [Fig. 5(a)] and the  $C_p$  data gradually increases and reaches a broad maximum ( $T^{\max}$ ) at 0.3 K. The presence of magnetic contribution to the heat capacity over a broad temperature range 3–0.09 K indicates the onset of short-range spin correlations from the 2D square-lattice spin network of  $J_{\text{eff}} = \frac{1}{2}$  magnetic moments. The broad maximum in the heat capacity data seems to be a common feature in various 2D Yb-based magnetic materials, as listed in Table I.

The  $C_p$  of magnetic insulators have a significant phononic contribution  $C_{\text{ph}}$  at high temperatures. While reaching low temperatures, the magnetic component of heat capacity  $C_m$

TABLE I. Details of various 2D layered Yb-based compounds.

Compound	$\theta_{CW}^{LT}$ (K)	Upturn in $C_p$	$T^{\max}$ (K) in $C_m$
YbMgGaO <sub>4</sub>	-4	10 K	2.4 [52]
NaYbO <sub>2</sub>	-5.6	11 K	1 [36]
YbZnGaO <sub>4</sub>	-2.7	10 K	1.8 [53]
BiYbGeO <sub>5</sub>	-0.6	6 K	0.6 [47]
Bi <sub>2</sub> YbO <sub>4</sub> Cl	-1	3 K	0.3

takes precedence over  $C_{\text{ph}}$ . As a result, the magnetic component of heat capacity can be set apart from the phononic component, especially for magnetic materials with low-energy scales of exchange couplings between magnetic moments.

To extract the  $C_m$  from  $C_p$  data, we initially estimated the phononic contribution by fitting the high- $T$  data via one Debye and one Einstein term [49],

$$C_{\text{ph}}(T) = f_D C_D(\theta_D, T) + g_E C_E(\theta_E, T). \quad (2)$$

The first term in Eq. (3) represents the Debye model,

$$C_D(\theta_D, T) = 9nR \left( \frac{T}{\theta_D} \right)^3 \int_0^{\frac{\theta_D}{T}} \frac{x^4 e^x}{(e^x - 1)^2} dx, \quad (3)$$

where  $x = \frac{\hbar\omega}{k_B T}$ ,  $\omega$  is the Debye frequency,  $R$  is the universal gas constant, and  $\theta_D$  represents the Debye temperature. The subsequent term of Eq. (3) is known as the Einstein term, and it accounts for the lattice vibrations of the flat optical modes,

$$C_E(\theta_E, T) = 3nR \left( \frac{\theta_E}{T} \right)^2 \frac{e^{\frac{\theta_E}{T}}}{[e^{\frac{\theta_E}{T}} - 1]^2}. \quad (4)$$

The characteristic Einstein temperature is denoted by  $\theta_E$ . The coefficients  $f_D$ , and  $g_E$  are the multiplication factors. The zero field  $C_p(T)$  data is fitted from 18 K to 225 K, using Eq. (3) [see Fig. 5(a)]. The obtained parameters are  $f_D \approx 0.45 \pm 0.05$ ,  $g_E \approx 0.54 \pm 0.05$ ,  $\theta_D \approx 240 \pm 2$  K, and  $\theta_E \approx 633 \pm 2$  K. The fit is further extrapolated to low temperatures down to 0.09 K. Finally,  $C_m(T)$  was obtained by subtracting the estimated lattice contribution from the measured  $C_p(T)$  data. The magnetic heat capacity  $C_m(T)$  at zero field is depicted in Fig. 5(b). The  $C_m(T)$  shows a broad maximum, from which the data falls steeply towards zero. We have attempted to fit with two-level Schottky model [49] on the  $C_m$  data at 0 T. We noticed that there is a significant mismatch between the fit and data at the low- $T$  region [see Fig. 5(b)], which rules out the presence of Schottky behavior in the  $C_m$  data at 0 T. The estimated  $C_m(T)$  is then used to calculate the change in magnetic entropy  $\Delta S_m$  by integrating  $C_m/T$  over  $T$  [see the inset of Fig. 5(a)]. The  $\Delta S_m$  value reaches saturation at 3.10 J/mol K in zero fields, which is almost 54% of the  $R \ln 2$  expected for  $J_{\text{eff}} = \frac{1}{2}$ . This result indicates that the remaining 46% of the entropy is getting released below 0.09 K due to the persistence of strong magnetic correlation; this similar reduction in entropy has also been observed in a few other Yb-based materials [48,54].

Furthermore, we measured the heat capacity data down to 1.8 K in several magnetic fields, and we identified a broad peak in the presence of magnetic fields, which tends to shift towards high temperatures with increasing field values due to

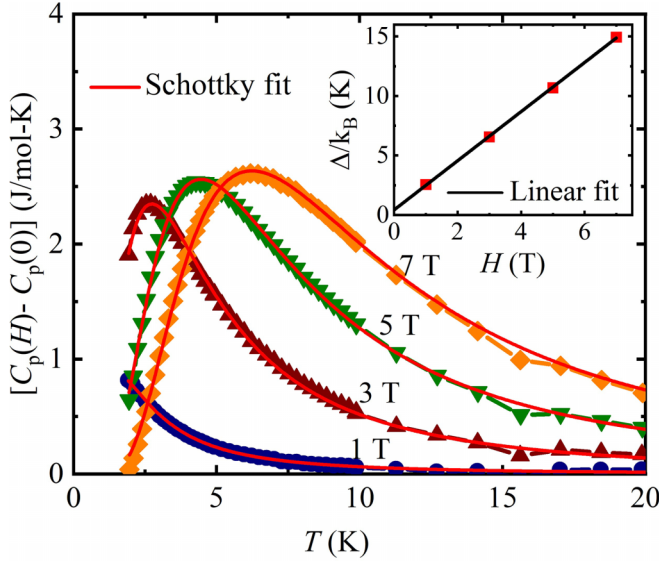


FIG. 6. Plot of  $[C_p(H) - C_p(0)]$  vs  $T$  at various fields with Schottky fit. (Inset) Plot of  $\Delta/k_B$  vs  $H$ , where the solid black line represents the linear fit.

the Zeeman splitting of the ground state Kramers doublet. The heat capacity data at various field values is fitted with a two-level Schottky fit (see Fig. 6). The Zeeman energy gap ( $\Delta$ ) between the energy levels of the ground-state Kramers doublet  $J = \pm \frac{1}{2}$  is extracted from the two-level Schottky fit, which increases linearly with the applied magnetic fields (see inset of Fig. 6). The linear dependence of the Zeeman energy gap with respect to the magnetic field is fitted with the expression  $\Delta = g\mu_B H$ ; the extracted parameter from the slope of the fit gives us  $g \approx 3.1$ , which is in good agreement with the value obtained through the magnetic measurements. Overall, the lack of LRO and the presence of short-range correlations in the heat capacity data suggests that the  $J_{\text{eff}} = \frac{1}{2}$  square-lattice spin system might possess a quantum disordered ground state.

#### IV. THEORETICAL RESULTS

In order to gain further insight into the interactions between  $\text{Yb}^{3+}$  ions, the effect of spin-orbit coupling, and the magnetic anisotropy, we investigate the electronic structure of  $\text{Bi}_2\text{YbO}_4\text{Cl}$ , computed within the DFT framework, which is discussed below.

##### A. Basic electronic structure

We start by describing the basic electronic structure of  $\text{Bi}_2\text{YbO}_4\text{Cl}$  within the nonmagnetic configuration. The computed nonspin-polarized band structure along the various high symmetry points of the Brillouin zone of  $\text{Bi}_2\text{YbO}_4\text{Cl}$  and the corresponding total and partial density of states (DOS) are shown in Figs. 7(a) and 7(b). As seen from Fig. 7(a), around the Fermi energy ( $E_F$ ), there is an isolated manifold of seven weakly dispersed bands. As evident from the partial Yb- $f$  DOS in Fig. 7(b), these bands have a predominant Yb- $f$  character. This can also be understood from the fact that the Yb ions are in the  $3+$  charge state with almost completely filled ( $\text{Yb}^{3+}:[\text{Xe}]4f^{13}$ )  $4f$  states. The DOS, below that regime [around the energy range  $-1$  to  $-5$  eV in Fig. 7(b)] is dom-

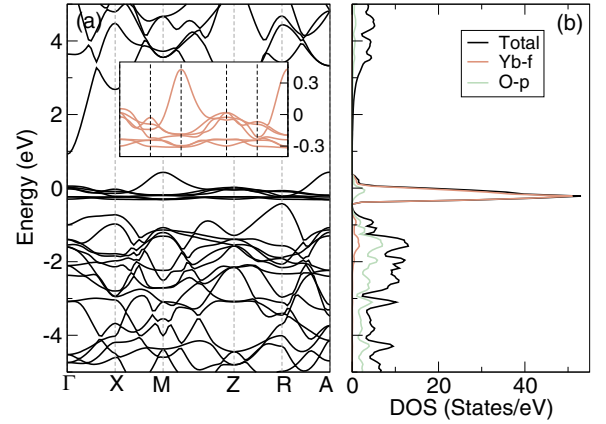


FIG. 7. The nonspin polarized electronic structure of  $\text{Bi}_2\text{YbO}_4\text{Cl}$ . (a) The band structure along the various high symmetry points of the Brillouin zone. The inset shows the zoomed-in isolated manifold of seven bands across the Fermi energy. (b) The total and the partial DOS, corresponding to the Yb- $f$  and the O- $p$  states, in  $\text{Bi}_2\text{YbO}_4\text{Cl}$ . The zero energy corresponds to the Fermi energy.

inated by the filled O- $p$  states ( $\text{O}^{2-}:[\text{He}]2s^22p^6$ ). The weak hybridization between Yb- $f$  and O- $p$  states is also evident from the partial DOS plot in Fig. 7(b). Since this isolated manifold of seven Yb- $f$  bands is responsible for the low-energy physics of the material, we construct a low-energy model Hamiltonian in the basis set of the seven Yb- $f$  states by downfolding the effect of the other orbitals using the  $N^{\text{th}}$  order muffin-tin orbital (NMTO) downfolding technique [55]. The on-site energies and  $f$ - $f$  hopping parameters are extracted in this process. The diagonalization of the computed on-site energies obtained in this method shows that the top-most valence band has predominant orbital contributions coming from  $f_x(5z^2 - 1)$  and  $f_x(3y^2 - x^2)$  orbitals.

The computed intra- and interplaner hopping integrals [see Fig. 2(a)] between these  $f$  orbitals are listed in Table II. We

TABLE II. The list of computed intra- and interplaner hopping integrals,  $t_{\alpha\beta}^{\text{intra}}$  and  $t_{\alpha\beta}^{\text{inter}}$ , between the Yb- $f$  orbitals,  $f_x(5z^2 - 1)$  and  $f_x(3y^2 - x^2)$ , indicated by the orbital indices  $\alpha$  and  $\beta$ . The connecting vectors between the neighboring Yb ions are also indicated in the table. For the intraplaner hopping  $t_{\alpha\beta}^{\text{intra}}$ , the magnitude of the hopping integrals depend on the direction of the hopping and are listed separately.

Hopping (meV)	$t_{\alpha\beta}^{\text{intra}} : (\pm a, 0, 0)$ $f_x(5z^2 - 1)$	$f_x(3y^2 - x^2)$
$f_x(5z^2 - 1)$	45	29
$f_x(3y^2 - x^2)$	29	-4
Hopping (meV)	$t_{\alpha\beta}^{\text{intra}} : (0, \pm a, 0)$ $f_x(5z^2 - 1)$	$f_x(3y^2 - x^2)$
$f_x(5z^2 - 1)$	0	-1
$f_x(3y^2 - x^2)$	-1	24
Hopping (meV)	$t_{\alpha\beta}^{\text{inter}} : (0, 0, \pm c)$ $f_x(5z^2 - 1)$	$f_x(3y^2 - x^2)$
$f_x(5z^2 - 1)$	0	0
$f_x(3y^2 - x^2)$	0	-4

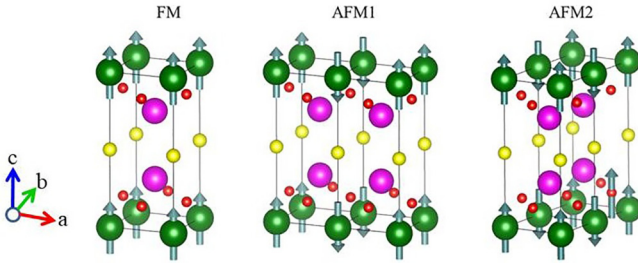


FIG. 8. The FM, AFM1, and AFM2 magnetic configurations of Bi<sub>2</sub>YbO<sub>4</sub>Cl. The arrows indicate the direction of the magnetic moment at the Yb<sup>3+</sup> ions.

note that the magnitude of the hopping integrals significantly reduces after the NN, as expected due to the localized nature of the  $f$  states, and consequently, the interplaner hopping  $t_{\alpha\beta}^{\text{inter}}$  is negligibly weak in magnitude (see Table II). Since the out-of-plane interactions between the Yb<sup>3+</sup> ions are extremely weak and the NN in-plane Yb<sup>3+</sup> ions with significant interactions form a square lattice, a two-dimensional spin model would be relevant for the description of the system. It is important to point out that the NN hopping integrals are *not* identical along  $\hat{x}$  and  $\hat{y}$ , as evident from the listed hopping integrals in Table II. The difference in hopping integrals, despite being equidistant, may be ascribed to the shape of the participating  $f$  orbitals along a particular direction of the hopping [56]. Our calculations, therefore, point out a direction-dependent NN hopping between the Yb<sup>3+</sup> ions.

### B. Effect of magnetism and spin-orbit interaction

Next, to understand the nature of magnetism between the Yb<sup>3+</sup> ions in Bi<sub>2</sub>YbO<sub>4</sub>Cl, we explicitly consider the effect of magnetism and perform the total energy calculations within the LDA +  $U$  formalism. For these calculations, we consider both ferromagnetic (FM) and antiferromagnetic (AFM) configurations with the neighboring Yb spins parallel and antiparallel to each other, respectively. Since the unit cell contains only one Yb ion, for the AFM configuration, we construct a  $2 \times 1 \times 1$  supercell and then keep the magnetic moments of the NN Yb<sup>3+</sup> ions (along  $\hat{x}$ ) antiparallel to each other. We refer to this AFM configuration as AFM1, which is shown in Fig. 8. We also construct a  $1 \times 2 \times 1$  supercell and keep the magnetic moments of the NN Yb<sup>3+</sup> ions antiparallel to each other along  $\hat{y}$ , as depicted in Fig. 8. We refer to this magnetic arrangement as AFM2 configuration. The computed total energies of the FM, AFM1, and AFM2 configurations, as listed in Table III, show that the FM configuration is lowest in energy, suggesting that the ferromagnetism is energetically favorable within the LDA +  $U$  formalism. The computed spin moment at the Yb<sup>3+</sup> ion for this configuration is  $0.97 \mu_B$ , consistent with the one unpaired electron remaining in the  $4f$  state of the Yb<sup>3+</sup> ion.

However, Yb atoms being heavy (large atomic number), it is also important to consider the effect of spin-orbit interaction in our calculations. We, therefore, compute the total energies of FM, AFM1, and AFM2 configurations in the presence of spin-orbit interaction, and the results of our calculations are also listed in Table III. Here, the spin polarization is along  $\hat{z}$ . In contrast to the case discussed above, in the presence of

TABLE III. Comparison of the total energies of the FM and AFM1 configurations along with the spin and orbital moments both in the absence and presence of SOC. The energy difference  $\Delta E$  is set to zero for the lower energy configuration. The orbital moment of the Yb ion is written in the parenthesis.

Magnetic config.	Without SOC	
	$\Delta E$ (meV)	Spin moment $\mu_B/\text{Yb}$
FM	0	0.97
AFM1	21	0.96
AFM2	4	0.97
Magnetic config.	With SOC	
	$\Delta E$ (meV)	Spin (orbital) moment $\mu_B/\text{Yb}$
FM	62	0.44 (1.02)
AFM1	0	0.77 (2.01)
AFM2	17	0.77 (2.01)

SOC, the AFM1 configuration becomes energetically more stable than the FM configuration (see Table III), suggesting that the SOC drives antiferromagnetism between the Yb ions. It is interesting to point out that such SOC-driven antiferromagnetism was also reported in the  $J_{\text{eff}} = \frac{1}{2}$  state of Ir-based  $5d$  transition metal oxide system [57]. Interestingly, the computed spin and orbital moments in the energetically lowest AFM1 configuration (see Table III) show that the orbital moment of the Yb<sup>3+</sup> ion is more than twice ( $\sim 2.6$ ) the value of the spin moment, which is a characteristic of the  $J_{\text{eff}} = \frac{1}{2}$  state. Our results, therefore, clearly show that the interaction between the Yb ions is of AFM in nature in agreement with the experimentally observed negative Curie-Weiss temperature  $\theta_{\text{CW}}$  and that the SOC plays a crucial role in driving the antiferromagnetism in the system. This leads to a two-dimensional AFM  $J_{\text{eff}} = \frac{1}{2}$  state in the system. The system is also insulating, in this case, consistent with the experimental results.

We note that the computed total energies of the AFM1 and AFM2 configurations, in which the NN Yb<sup>3+</sup> ions along  $\hat{x}$  and  $\hat{y}$  have antiparallel spin arrangements respectively, are different. In particular, the computed total energy for the AFM2 configuration is found to be higher than that of the AFM1 configuration by about 17 meV/f.u. This difference in total energy may be attributed to the different magnitudes of the NN hopping along  $\hat{x}$  and  $\hat{y}$ . We further note that the AFM1 configuration is lower in energy, consistent with the overall larger NN hopping integrals along  $\hat{x}$  than  $\hat{y}$ , as listed in Table II. The difference in the AFM1 and AFM2 configurations may also suggest a deviation from the simple Heisenberg model, pointing towards the existence of more complex higher-order exchange couplings. Exploring this aspect could be an interesting direction for future work.

### C. Magnetic anisotropy

To gain further insight into the orientation of the magnetic moment at the Yb<sup>3+</sup> ions, we first identify the allowed

TABLE IV. Energy differences  $\Delta E$  of the AFM1 configuration for different orientations of the magnetic moment with respect to the case when the moment is along  $\hat{z}$  (001). The corresponding spin and orbital moments are also listed.

Magnetic moments along	$\Delta E$ (meV)	Spin (orbital) moment $\mu_B/\text{Yb}$
(100)	4	0.78 (2.08)
(010)	45	0.78 (2.08)
(001)	0	0.77 (2.01)

magnetic space groups for the  $P4/mmm$  symmetry of the crystal structure of  $\text{Bi}_2\text{YbO}_4\text{Cl}$  using MAXMAGN, as implemented in the Bilbao crystallographic server [58]. Note that this analysis depends on the propagation vector  $\vec{k}$ . Since the results of our calculations in the previous section show that the AFM1 configuration, corresponding to the  $2 \times 1 \times 1$  magnetic supercell, has the lowest energy among the considered magnetic configurations, we restrict our analysis here to the propagation vector  $\vec{k} = (1/2, 0, 0)$ . We find that for this given propagation vector, the structural space group  $P4/mmm$  allows for only three magnetic space groups with nonzero magnetic moments at the Yb ions. All these allowed magnetic space groups dictate an AFM arrangement of the magnetic moments at the  $\text{Yb}^{3+}$  ions, with three different orientations of the magnetic moment, viz.,  $\hat{x}$  (100),  $\hat{y}$  (010), and  $\hat{z}$  (001).

Guided by this symmetry analysis, we next carried out total energy calculations within the LDA + SOC +  $U$  framework for the same AFM1 configuration but aligning the magnetic moments along  $\hat{x}$  and  $\hat{y}$ , in addition to the previous case (see Sec. IV B) with moments along  $\hat{z}$ . The results of our calculations are listed in Table IV. The comparison of the total energies clearly shows that the Yb magnetic moments prefer to align along  $\hat{z}$  (001), indicating an easy-axis (out-of-plane) anisotropy in  $\text{Bi}_2\text{YbO}_4\text{Cl}$ . We hope that our work will motivate future research in exploring the ground state of the ideal 2D HAFM model and its deviation due to the influence of SOC, offering avenues for research on quantum magnetism.

## V. CONCLUSIONS

In summary, we synthesized, examined the magnetic properties, and calculated the electronic structure of a compound  $\text{Bi}_2\text{YbO}_4\text{Cl}$  with a structurally perfect 2D square-lattice network of  $\text{Yb}^{3+}$  ions. Our findings show that  $\text{Yb}^{3+}$  ions host  $J_{\text{eff}} = \frac{1}{2}$  moments. The antiferromagnetic interaction between the  $J_{\text{eff}} = \frac{1}{2}$  moments are identified with a Curie-Weiss temperature of about  $-1 \pm 0.1$  K. The heat capacity data exhibit a broad maximum at 0.3 K, suggesting the presence of short-range correlations. There is no indication of any sharp magnetic anomaly in the heat capacity data down to 0.09 K. The titled compound is resistant in exhibiting the magnetic LRO even at very low temperatures (relative to the  $\theta_{\text{CW}}^{LT}$  value of about  $-1$  K), which is attributed to the presence of strong quantum fluctuations resulting from the low dimensionality and spin-orbit coupling. Our total energy calculations also demonstrate that the NN Yb- $f$  electrons interact antiferromagnetically. The spin-orbit interaction drives the antiferromagnetic interaction, and the estimated spin and orbital moments suggest the presence of a  $J_{\text{eff}} = \frac{1}{2}$  state. The total energy calculation indicates that the system is a spin-orbit coupled Mott-Hubbard insulator with easy-axis (out-of-plane) anisotropy. Further, the  $\mu\text{SR}$  and INS investigations would help unveil the true nature of the excitations of the titled compound. In addition, the theoretical endeavors to explore the potential existence of non-Heisenberg-like, highly anisotropic spin interactions [34] could offer crucial insights into understanding the magnetic ground state of  $\text{Bi}_2\text{YbO}_4\text{Cl}$ .

## ACKNOWLEDGMENTS

B.K. acknowledges support from DST SERB grant (CRG/2023/003063). S.B. thanks ETH Zurich for financial support. P.K. acknowledges the funding by the Science and Engineering Research Board and the Department of Science and Technology, India, through research grants. The work at SNU was supported by the NRF through the Quantum Computing Research Infrastructure Construction Program (2022M3K2A1083855) and by the Ministry of Education through the core center Program (2021R1A6C101B418)

- [1] J. G. Bednorz and K. A. Müller, Possible high  $T_c$  superconductivity in the Ba-La-Cu-O system, *Z. Phys. B* **64**, 189 (1986).
- [2] A. N. Vasiliev, O. S. Volkova, E. A. Zvereva, and M. Markina, Milestones of low-D quantum magnetism, *npj Quantum Mater.* **3**, 18 (2018).
- [3] N. D. Mermin and H. Wagner, Absence of ferromagnetism or antiferromagnetism in one- or two-dimensional isotropic Heisenberg models, *Phys. Rev. Lett.* **17**, 1133 (1966).
- [4] S. Sachdev, *Quantum Phase Transitions* (Cambridge University Press, Cambridge, 1999).
- [5] R. Y. Q. Si and E. Abrahams, High-temperature superconductivity in iron pnictides and chalcogenides, *Nat. Rev. Mater.* **1**, 16017 (2016).
- [6] M. Wang, C. Zhang, X. Lu, G. Tan, H. Luo, Y. Song, M. Wang, X. Zhang, E. Goremychkin, T. Perring *et al.*, Doping

dependence of spin excitations and its correlations with high-temperature superconductivity in iron pnictides, *Nat. Commun.* **4**, 2874 (2013).

- [7] D. Li, K. Lee, B. Y. Wang, M. Osada, S. Crossley, H. R. Lee, Y. Cui, Y. Hikita, and H. Y. Hwang, Superconductivity in an infinite-layer nickelate, *Nature (London)* **572**, 624 (2019).
- [8] S. Zeng, C. S. Tang, X. Yin, C. Li, M. Li, Z. Huang, J. Hu, W. Liu, G. J. Omar, H. Jani, Z. S. Lim, K. Han, D. Wan, P. Yang, S. J. Pennycook, A. T. S. Wee, and A. Ariando, Phase diagram and superconducting dome of infinite-layer  $\text{Nd}_{1-x}\text{Sr}_x\text{NiO}_2$  thin films, *Phys. Rev. Lett.* **125**, 147003 (2020).
- [9] J. D. Reger and A. P. Young, Monte Carlo simulations of the spin- $(1/2)$  Heisenberg antiferromagnet on a square lattice, *Phys. Rev. B* **37**, 5978 (1988).



- [10] R. Coldea, S. M. Hayden, G. Aeppli, T. G. Perring, C. D. Frost, T. E. Mason, S.-W. Cheong, and Z. Fisk, Spin waves and electronic interactions in La<sub>2</sub> CuO<sub>4</sub>, *Phys. Rev. Lett.* **86**, 5377 (2001).
- [11] N. S. Headings, S. M. Hayden, R. Coldea, and T. G. Perring, Anomalous high-energy spin excitations in the high- $T_c$  superconductor-parent antiferromagnet La<sub>2</sub> CuO<sub>4</sub>, *Phys. Rev. Lett.* **105**, 247001 (2010).
- [12] M. Greven, R. Birgeneau, Y. Endoh, M. Kastner, M. Matsuda, and G. Shirane, Neutron scattering study of the two-dimensional spin  $S = 1/2$  square-lattice Heisenberg antiferromagnet Sr<sub>2</sub>CuO<sub>2</sub>Cl<sub>2</sub>, *Z. Phys. B* **96**, 465 (1995).
- [13] K. W. Plumb, A. T. Savici, G. E. Granroth, F. C. Chou, and Y.-J. Kim, High-energy continuum of magnetic excitations in the two-dimensional quantum antiferromagnet Sr<sub>2</sub>CuO<sub>2</sub>Cl<sub>2</sub>, *Phys. Rev. B* **89**, 180410(R) (2014).
- [14] N. B. Christensen, H. M. Rønnow, D. F. McMorrow, A. Harrison, T. Perring, M. Enderle, R. Coldea, L. Regnault, and G. Aeppli, Quantum dynamics and entanglement of spins on a square lattice, *Proc. Natl. Acad. Sci. USA* **104**, 15264 (2007).
- [15] B. Dalla Piazza, M. Mourigal, N. B. Christensen, G. Nilson, P. Tregenna-Piggott, T. Perring, M. Enderle, D. F. McMorrow, D. Ivanov, and H. M. Rønnow, Fractional excitations in the square-lattice quantum antiferromagnet, *Nat. Phys.* **11**, 62 (2015).
- [16] H. Shao, Y. Q. Qin, S. Capponi, S. Chesi, Z. Y. Meng, and A. W. Sandvik, Nearly deconfined spinon excitations in the square-lattice spin-1/2 Heisenberg antiferromagnet, *Phys. Rev. X* **7**, 041072 (2017).
- [17] L. Martinelli, D. Betto, K. Kummer, R. Arpaia, L. Braicovich, D. Di Castro, N. B. Brookes, M. Moretti Sala, and G. Ghiringhelli, Fractional spin excitations in the infinite-layer cuprate CaCuO<sub>2</sub>, *Phys. Rev. X* **12**, 021041 (2022).
- [18] P. W. Anderson, The resonating valence bond state in La<sub>2</sub>CuO<sub>4</sub> and superconductivity, *Science* **235**, 1196 (1987).
- [19] G. Shirane, Y. Endoh, R. J. Birgeneau, M. A. Kastner, Y. Hidaka, M. Oda, M. Suzuki, and T. Murakami, Two-dimensional antiferromagnetic quantum spin-fluid state in La<sub>2</sub>CuO<sub>4</sub>, *Phys. Rev. Lett.* **59**, 1613 (1987).
- [20] A. W. Sandvik, Evidence for deconfined quantum criticality in a two-dimensional Heisenberg model with four-spin interactions, *Phys. Rev. Lett.* **98**, 227202 (2007).
- [21] T. Roscilde, P. Verrucchi, A. Fubini, S. Haas, and V. Tognetti, Entanglement and factorized ground states in two-dimensional quantum antiferromagnets, *Phys. Rev. Lett.* **94**, 147208 (2005).
- [22] Y. Li, P. Gegenwart, and A. A. Tsirlin, Spin liquids in geometrically perfect triangular antiferromagnets, *J. Phys.: Condens. Matter* **32**, 224004 (2020).
- [23] J. D. Thompson, P. A. McClarty, and M. J. P. Gingras, Local susceptibility of the Yb<sub>2</sub>Ti<sub>2</sub>O<sub>7</sub> rare earth pyrochlore computed from a Hamiltonian with anisotropic exchange, *J. Phys.: Condens. Matter* **23**, 164219 (2011).
- [24] K. A. Ross, L. Savary, B. D. Gaulin, and L. Balents, Quantum excitations in quantum spin ice, *Phys. Rev. X* **1**, 021002 (2011).
- [25] J. D. Thompson, P. A. McClarty, H. M. Rønnow, L. P. Regnault, A. Sorge, and M. J. P. Gingras, Rods of neutron scattering intensity in Yb<sub>2</sub>Ti<sub>2</sub>O<sub>7</sub>: Compelling evidence for significant anisotropic exchange in a magnetic pyrochlore oxide, *Phys. Rev. Lett.* **106**, 187202 (2011).
- [26] J. D. Thompson, P. A. McClarty, D. Prabhakaran, I. Cabrera, T. Guidi, and R. Coldea, Quasiparticle breakdown and spin hamiltonian of the frustrated quantum pyrochlore Yb<sub>2</sub>Ti<sub>2</sub>O<sub>7</sub> in a magnetic field, *Phys. Rev. Lett.* **119**, 057203 (2017).
- [27] L. S. Wu, S. E. Nikitin, Z. Wang, W. Zhu, C. D. Batista, A. M. Tsvelik, A. M. Samarakoon, D. A. Tennant, M. Brando, L. Vasylychko *et al.*, Tomonaga–Luttinger liquid behavior and spinon confinement in YbAlO<sub>3</sub>, *Nat. Commun.* **10**, 698 (2019).
- [28] J. G. Rau and M. J. P. Gingras, Frustration and anisotropic exchange in ytterbium magnets with edge-shared octahedra, *Phys. Rev. B* **98**, 054408 (2018).
- [29] J. Xing, E. Feng, Y. Liu, E. Emmanouilidou, C. Hu, J. Liu, D. Graf, A. P. Ramirez, G. Chen, H. Cao, and N. Ni, Néel-type antiferromagnetic order and magnetic field–temperature phase diagram in the spin- $\frac{1}{2}$  rare-earth honeycomb compound YbCl<sub>3</sub>, *Phys. Rev. B* **102**, 014427 (2020).
- [30] G. Sala, M. B. Stone, B. K. Rai, A. F. May, P. Laurell, V. O. Garlea, N. P. Butch, M. D. Lumsden, G. Ehlers, G. Pokharel *et al.*, Van Hove singularity in the magnon spectrum of the antiferromagnetic quantum honeycomb lattice, *Nat. Commun.* **12**, 171 (2021).
- [31] Z. Zhang, Y. Cai, J. Kang, Z. Ouyang, Z. Zhang, A. Zhang, J. Ji, F. Jin, and Q. Zhang, Anisotropic exchange coupling and ground state phase diagram of Kitaev compound YbOCl, *Phys. Rev. Res.* **4**, 033006 (2022).
- [32] L. Capriotti, A. E. Trumper, and S. Sorella, Long-range néel order in the triangular Heisenberg model, *Phys. Rev. Lett.* **82**, 3899 (1999).
- [33] S. R. White and A. L. Chernyshev, Néel order in square and triangular lattice Heisenberg models, *Phys. Rev. Lett.* **99**, 127004 (2007).
- [34] Y. Li, G. Chen, W. Tong, L. Pi, J. Liu, Z. Yang, X. Wang, and Q. Zhang, Rare-earth triangular lattice spin liquid: A single-crystal study of YbMgGaO<sub>4</sub>, *Phys. Rev. Lett.* **115**, 167203 (2015).
- [35] Y. Xu, J. Zhang, Y. S. Li, Y. J. Yu, X. C. Hong, Q. M. Zhang, and S. Y. Li, Absence of magnetic thermal conductivity in the quantum spin-liquid candidate YbMgGaO<sub>4</sub>, *Phys. Rev. Lett.* **117**, 267202 (2016).
- [36] L. Ding, P. Manuel, S. Bachus, F. Grubler, P. Gegenwart, J. Singleton, R. D. Johnson, H. C. Walker, D. T. Adroja, A. D. Hillier, and A. A. Tsirlin, Gapless spin-liquid state in the structurally disorder-free triangular antiferromagnet NaYbO<sub>2</sub>, *Phys. Rev. B* **100**, 144432 (2019).
- [37] R. Sarkar, P. Schlender, V. Grinenko, E. Haeussler, P. J. Baker, T. Doert, and H.-H. Klauss, Quantum spin liquid ground state in the disorder free triangular lattice NaYbS<sub>2</sub>, *Phys. Rev. B* **100**, 241116(R) (2019).
- [38] E. Manousakis, The spin-1/2 Heisenberg antiferromagnet on a square lattice and its application to the cuprous oxides, *Rev. Mod. Phys.* **63**, 1 (1991).
- [39] U. Arjun, K. Ranjith, A. Jesche, F. Hirschberger, D. Sarma, and P. Gegenwart, Adiabatic demagnetization refrigeration to millikelvin temperatures with the distorted square lattice magnet NaYbGeO<sub>4</sub>, *Phys. Rev. B* **108**, 224415 (2023).
- [40] M. Schmidt, H. Oppermann, C. Hennig, R. W. Henn, E. Gmelin, N. Söger, and M. Binnewies, Untersuchungen zu bismut-seltenerdoxidhalogeniden der zusammensetzung Bi<sub>2</sub>SeO<sub>4</sub>X (SE = Y, La-Lu, X = Cl, Br, I), *Z. Anorg. Allg. Chem.* **626**, 125 (2000).
- [41] J. Rodríguez-Carvajal, Recent advances in magnetic structure determination by neutron powder diffraction, *Phys. B: Condens. Matter* **192**, 55 (1993).

- [42] The Elk Code, <http://elk.sourceforge.net/>.
- [43] D.-Y. Zheng, Z.-X. Shen, M. Zhang, and L. He, First-principles study of magnetic structures of triangular antiferromagnets  $\text{NaYbS}_2$  and  $\text{NaYbO}_2$ , [arXiv:2104.09739](https://arxiv.org/abs/2104.09739).
- [44] X. Gui, T.-R. Chang, K. Wei, M. J. Daum, D. E. Graf, R. E. Baumbach, M. Mourigal, and W. Xie, A novel magnetic material by design: Observation of  $\text{Yb}^{3+}$  with spin-1/2 in  $\text{Yb}_x\text{Pt}_5\text{P}$ , *ACS Central Sci.* **6**, 2023 (2020).
- [45] P. W. Selwood, *Magnetochemistry*, 2nd ed. (Interscience publishers, New York, 1956).
- [46] U. K. Voma, S. Bhattacharya, E. Kermarrec, J. Alam, Y. M. Jana, B. Sana, P. Khuntia, S. K. Panda, and B. Koteswararao, Electronic structure and magnetic properties of the effective spin  $\text{K}_3\text{Yb}(\text{VO}_4)_2$ , *Phys. Rev. B* **104**, 144411 (2021).
- [47] S. Mohanty, S. S. Islam, N. Winterhalter-Stocker, A. Jesche, G. Simutis, C. Wang, Z. Guguchia, J. Sichelschmidt, M. Baenitz, A. A. Tsirlin, P. Gegenwart, and R. Nath, Disordered ground state in the spin-orbit coupled  $J_{\text{eff}} = \frac{1}{2}$  distorted honeycomb magnet  $\text{BiYbGeO}_5$ , *Phys. Rev. B* **108**, 134408 (2023).
- [48] K. Somesh, S. S. Islam, S. Mohanty, G. Simutis, Z. Guguchia, C. Wang, J. Sichelschmidt, M. Baenitz, and R. Nath, Absence of magnetic order and emergence of unconventional fluctuations in the  $J_{\text{eff}} = \frac{1}{2}$  triangular-lattice antiferromagnet  $\text{YbBO}_3$ , *Phys. Rev. B* **107**, 064421 (2023).
- [49] C. Kittel and P. McEuen, *Introduction to Solid State Physics* (John Wiley & Sons, Hoboken, NJ, 2018).
- [50] S. Mugiraneza and A. M. Hallas, Tutorial: A beginner's guide to interpreting magnetic susceptibility data with the Curie-Weiss law, *Commun. Phys.* **5**, 95 (2022).
- [51] U. Arjun, K. M. Ranjith, A. Jesche, F. Hirschberger, D. D. Sarma, and P. Gegenwart, Efficient adiabatic demagnetization refrigeration to below 50 mK with ultrahigh-vacuum-compatible ytterbium diphosphates  $\text{AYbP}_2\text{O}_7$  ( $A = \text{Na}, \text{K}$ ), *Phys. Rev. Appl.* **20**, 014013 (2023).
- [52] Y. Li, H. Liao, Z. Zhang, S. Li, F. Jin, L. Ling, L. Zhang, Y. Zou, L. Pi, Z. Yang *et al.*, Gapless quantum spin liquid ground state in the two-dimensional spin-1/2 triangular antiferromagnet  $\text{YbMgGaO}_4$ , *Sci. Rep.* **5**, 16419 (2015).
- [53] Z. Ma, J. Wang, Z.-Y. Dong, J. Zhang, S. Li, S.-H. Zheng, Y. Yu, W. Wang, L. Che, K. Ran, S. Bao, Z. Cai, P. Čermák, A. Schneidewind, S. Yano, J. S. Gardner, X. Lu, S.-L. Yu, J.-M. Liu, S. Li *et al.*, Spin-glass ground state in a triangular-lattice compound  $\text{YbZnGaO}_4$ , *Phys. Rev. Lett.* **120**, 087201 (2018).
- [54] B. Sana, M. Barik, M. Pregelj, U. Jena, M. Baenitz, J. Sichelschmidt, K. Sethupathi, and P. Khuntia, Magnetic properties of a spin-orbit entangled  $J_{\text{eff}} = \frac{1}{2}$  three-dimensional frustrated rare-earth hyperkagome material, *Phys. Rev. B* **108**, 134413 (2023).
- [55] O. K. Andersen and T. Saha-Dasgupta, Muffin-tin orbitals of arbitrary order, *Phys. Rev. B* **62**, R16219 (2000).
- [56] K. Takegahara, Y. Aoki, and A. Yanase, Slater-Koster tables for  $f$  electrons, *J. Phys. C: Solid State Phys.* **13**, 583 (1980).
- [57] S. Bhowal, S. Ganguly, and I. Dasgupta, Spin-orbit coupling driven novel magnetism in  $d^5$  6H-perovskite iridates  $\text{Ti}_2\text{O}_9$  and  $\text{Ba}_3\text{TiIr}_2\text{O}_9$ , *J. Phys.: Condens. Matter* **31**, 185802 (2019).
- [58] J. Perez-Mato, S. Gallego, E. Tasci, L. Elcoro, G. de la Flor, and M. Aroyo, Symmetry-based computational tools for magnetic crystallography, *Annu. Rev. Mater. Res.* **45**, 217 (2015).